Engineering synthetic gauge fields through the coupling phases in cavity magnonics

Alan Gardin,[1,2,*] Guillaume Bourcin,[2] Jeremy Bourhill,[3] Vincent Vlaminck,[2] Christian Person,[2] Christophe Fumeaux,[4] Giuseppe C. Tettamanzi,[1,5] and Vincent Castel[2]

[1] *School of Physics, The University of Adelaide, Adelaide, SA 5005, Australia*

[2] *Lab-STICC, UMR CNRS 6285, IMT Atlantique, Brest F-29238, France*

[3] *ARC Centre of Excellence for Engineered Quantum Systems and ARC Centre of Excellence for Dark Matter Particle Physics, Department of Physics, University of Western Australia, 35 Stirling Highway, Crawley, WA 6009, Australia*

[4] *School of Electrical Engineering and Computer Science, The University of Queensland, Brisbane, QLD 4072, Australia*

[5] *School of Chemical Engineering and Advanced Materials, The University of Adelaide, Adelaide, SA 5005, Australia*

(Received 13 December 2023; revised 6 May 2024; accepted 17 May 2024; published 13 June 2024)

Cavity magnonics, which studies the interaction of light with magnetic systems in a cavity, is a promising platform for quantum transducers and quantum memories. At microwave frequencies, the coupling between a cavity photon and a magnon, the quasiparticle of a spin-wave excitation, is a consequence of the Zeeman interaction between the cavity's magnetic field and the magnet's macroscopic spin. For each photon-magnon interaction, a coupling phase factor exists, and this is often neglected in simple systems; however, in "loop-coupled" systems, where there are at least as many couplings as modes, the coupling phases become relevant for the physics and lead to synthetic gauge fields. We present experimental evidence of the existence of such coupling phases by considering two spheres made of yttrium-iron-garnet and two different re-entrant cavities. We predict numerically the values of the coupling phases, and we find good agreement between the theory and the experimental data. These results show that in cavity magnonics, one can engineer synthetic gauge fields, which can be useful for cavity-mediated coupling and engineering dark-mode physics.

DOI: 10.1103/PhysRevApplied.21.064033

I. INTRODUCTION

Magnons are the quasiparticles associated with the elementary excitation of a spin wave in a magnetically ordered material, such as the ferrimagnet yttrium-iron-garnet (YIG). The field of cavity magnonics, or spin cavitronics, aims to use the interactions of photons in a cavity with magnons for both classical technologies (e.g., radio-frequency circulators or isolators, and spintronics [1–10]) and quantum technologies [11–13]. Magnons are notably promising for quantum transduction [14] due to their capability to couple to phonons [15], optical and microwave photons, and superconducting qubits [16–19]. The coupling with microwave photons has been particularly fruitful, and there have been demonstrations of coherent coupling [20], indirect coupling [21,22], ultrastrong coherent coupling [23–27], dissipative coupling [28–36], the tuning between level repulsion and attraction [37,38], a dark-mode memory [39], and nonreciprocal effects [36,40–42].

Physically, all of these results involve the photon-magnon coupling, which originates from the Zeeman interaction between the magnetic dipole moment of a magnet and a magnetic field. This interaction is characterized by a coupling strength and a coupling phase, which can both be chosen to be real positive numbers. As recently shown in Ref. [43], in most simple systems, the coupling phases can be ignored since they do not affect the physics; however, in "loop-coupled" systems [42,44–49], where there are at least as many couplings as modes, neglecting the coupling phases can lead to an erroneous description of the physics. Notably, in the context of cavity magnonics, it has been theoretically shown that the coupling phases can steer the system toward either dark-mode physics (which is useful for quantum memories [39]) or the enhancement of cavity-mediated coupling by taking advantage of several cavity modes [43] (which is useful for quantum information transduction).

*Corresponding author: alan.gardin@adelaide.edu.au

However, so far, no experimental evidence of the coupling phases has been reported, despite their striking impact on cavity-magnonics applications. To bridge this gap, we propose two re-entrant three-post cavities, in which multiple cavity modes simultaneously couple to two magnon modes, creating loop-coupled systems. We experimentally measure a first cavity in which the physics is characterized by a single physical phase $\theta = \pi$, which makes it fall within the theoretical analysis of a previous work [43]. In contrast, in the second cavity, the physics is determined by two physical phases $\theta_1 = 0$ and $\theta_2 = \pi$. In both cavities, we predict theoretically the values of the physical phases and find good agreement with our experiments.

In Sec. II, we introduce the coupling phases, and how one can reduce them to the so-called *physical phases* characterizing the physics using unitary transformations. Importantly, we interpret these physical phases as parametrizing a synthetic $U(1)$ gauge field (or synthetic magnetic field), allowing our work to be connected to the wider literature. Next, in Sec. III, we introduce a cavity with a physical phase $\theta = \pi$, which is supported by both theory and experiment. In Sec. IV, we perform a similar analysis, but this time on a cavity leading to the physical phases $\theta_1 = \pi$ and $\theta_2 = 0$. We conclude in Sec. V.

II. INTRODUCTION TO THE MAGNON-PHOTON COUPLING PHASE

We adopt a second-quantized formalism for the description of the cavity (annihilation operator c_k) and magnon modes (annihilation operator m_l after performing the Holstein-Primakoff transformation [50] on the macrospin operator [51]). The ferromagnetic resonance frequency of the magnons is tuned by a static applied magnetic field $\mathbf{H}_0 = H_0\hat{\mathbf{z}}$. The coupling between the cavity mode c_k and the magnon mode m_l is characterized by a coupling strength $g_{kl}/2\pi$ and a coupling phase φ_{kl} defined as [43,51]

$$g_{kl}/2\pi = \eta_{kl}\sqrt{\omega_k}\frac{\gamma}{4\pi}\sqrt{\frac{\mu}{g_L\mu_B}\hbar\mu_0 n_s}, \tag{1}$$

$$\varphi_{kl} = \arg\left\{\int_{V_m} \mathrm{d}^3 r \mathbf{h}_k(\mathbf{r})\cdot\hat{\mathbf{x}} + i\int_{V_m} \mathrm{d}^3 r \mathbf{h}_k(\mathbf{r})\cdot\hat{\mathbf{y}}\right\}, \tag{2}$$

where $\gamma/2\pi = 28$ GHz/T is the gyromagnetic ratio, $\mu = 5\mu_B$ is the magnetic moment of a unit cell of YIG, μ_B is the Bohr magneton, μ_0 is the magnetic permeability of vacuum, $g_L = 2$ is the Landé g-factor, $n_s = 4.22\times 10^{23}$ m^{-3} is the spin density of YIG [52], $\mathbf{h}_k$ is the magnetic field vector of the cavity mode k, V_m is the volume of the YIG spheres, and

$$\eta_{kl} = \sqrt{\frac{\left(\int_{V_m} \mathrm{d}^3 r \mathbf{h}_k(\mathbf{r})\cdot\hat{\mathbf{x}}\right)^2 + \left(\int_{V_m} \mathrm{d}^3 r \mathbf{h}_k(\mathbf{r})\cdot\hat{\mathbf{y}}\right)^2}{V_m\int_{V_c}\mathrm{d}^3 r|\mathbf{h}_k(\mathbf{r})|^2}} \tag{3}$$

is the filling factor, in which V_c is the volume of the cavity.

The interaction Hamiltonian between the cavity mode c_k and the magnon mode m_l reads [43]

$$H_I = \hbar g_{kl}\left(e^{i\varphi_{kl}}c_k m_l^\dagger + e^{-i\varphi_{kl}}c_k^\dagger m_l\right), \tag{4}$$

in which we used the rotating-wave approximation, which is valid provided $(g_{kl}/\omega_k) < 10\%$ [53,54]. Note that the interaction Hamiltonian (4) is Hermitian and results from the coherent coupling between photons and magnons. This is in stark contrast with dissipative couplings [11,12], in which the interaction is non-Hermitian and results from an indirect coupling [55] of the magnons and photons through a strongly dissipative mode [28,29], or traveling wave reservoir [30–36].

Formally, recall that the unitary transformation $U = e^{i\varphi c^\dagger c}$ transforms the operator c as $c \mapsto e^{-i\varphi}c$, and that unitary transformations amount to a change of basis. Thus, the transformations $U_{c_k} = e^{i\varphi_{kl}c_k^\dagger c_k}$ and $U_{m_l} = e^{-i\varphi_{kl}m_l^\dagger m_l}$ can both remove the coupling phase from Eq. (4). Physically, this means that there exists a basis in which the coupling phase vanishes, so we might as well set it to zero to simplify the study of the physics. In other words, this amounts to changing the reference phase.

The situation is more complicated when one considers several simultaneous couplings. Naturally, any isolated bosonic mode has a local phase degree of freedom [corresponding to a $U(1)$ symmetry] since, for example, the mapping $c \mapsto e^{-i\varphi}c$ does not change its Hamiltonian; however, couplings between modes constrain these local phase choices, which can break this symmetry. For instance, the coupling of Eq. (4) "locks" the local phase choices of c_k and m_l together, but we are still free to rotate either c_k (using U_{c_k}) or m_l (using U_{m_l}) to remove the coupling phase. In other words, we have two phase degrees of freedom, but there is only one constraint between them; however, when the number of couplings (constraints) is greater than or equal to the number of modes (degrees of freedom), we cannot remove all the coupling phases, and they become relevant for the physics.

To illustrate this concept, let us consider the example of two magnon modes simultaneously coupling to three cavity modes, as illustrated in Fig. 1. We can eliminate the coupling phases between m_1 and the cavity modes in Fig. 1(a) using

$$U_{c_k} = e^{i\varphi_{k1}c_k^\dagger c_k}, \quad k \in \{1,2,3\}, \tag{5}$$

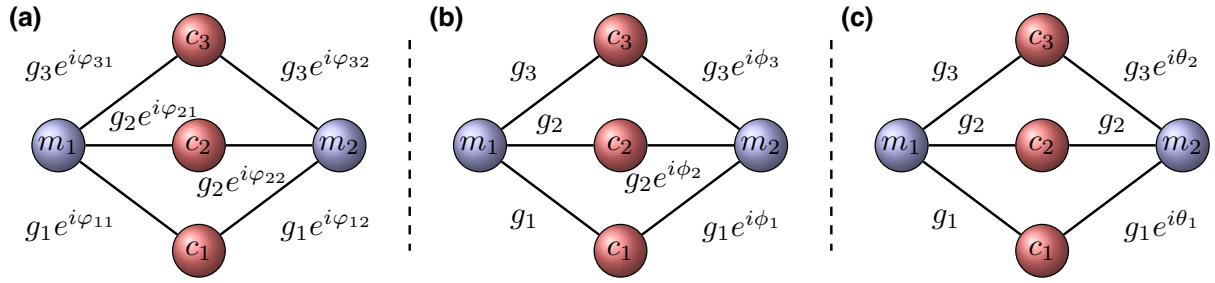

FIG. 1. Simplification of the physics of a system composed of two magnon modes m_1 and m_2 (in blue) coupling equally and simultaneously to three cavity modes c_1, c_2, and c_3 (in red). (a) The system in which all the coupling phases remain. (b) After unitarily transforming the cavity modes using Eq. (5), the physics is determined only by three phases $\phi_k = \varphi_{k2} - \varphi_{k1}$, accounting for the difference in coupling for each cavity mode $k \in \{1, 2, 3\}$. (c) After rotating m_2 using Eq. (6), we are left with two physical phases $\theta_1 = \phi_1 - \phi_2$ and $\theta_2 = \phi_3 - \phi_2$.

and we obtain Fig. 1(b). Next, we rotate m_2 with

$$U_{c_k} = e^{i\phi_2 m_2^\dagger m_2}, \tag{6}$$

and we finally obtain two *physical phases* θ_1 and θ_2 characterizing the physics [see Fig. 1(c)].

Therefore, in the system of Fig. 1, we have six couplings and five modes, leading to two physical phases. If the two magnons couple to only two cavity modes (e.g., by setting $g_3 = 0$), we have as many constraints as degrees of freedom, and the system is characterized by a single physical phase.

To conclude this section, we would like to mention that a physical phase effectively parametrizes an artificial (or synthetic) $U(1)$ gauge field. Indeed, Eq. (4) can be interpreted as the interaction Hamiltonian of a charged particle on a lattice in the presence of a static magnetic field (see Refs. [46,56] for instance). These artificial gauge fields have been proposed for several physical systems, such as neutral atoms [57,58], circuit QED [46,55,59], and cavity optomechanics [47–49]. Electrodynamics is naturally a $U(1)$ gauge theory, and therefore, by analogy, an artificial $U(1)$ gauge field leads to synthetic electromagnetism. Notably, an artificial magnetic field can be used to break time-reversal symmetry in systems where the presence of a "natural" magnetic field is problematic, such as in circuit QED [46]. In turn, synthetic gauge fields can be used to create nonreciprocal behaviors by balancing coherent and dissipative couplings through reservoir engineering [55,56,60], and there have been proposals for circuit QED [46,55,59] and cavity optomechanics [47–49]. Framing the effect of the coupling phases in cavity magnonics in terms of synthetic gauge fields allows a connection to be made with all the aforementioned works; however, it is worth noting that the associated applications may not be so relevant for cavity magnonics, because a static magnetic field is already present. Still, as shown in Ref. [43], the coupling phases, or the associated synthetic gauge field, can lead to distinct physics in cavity magnonics; therefore, their study remains of practical interest.

III. A SINGLE PHYSICAL PHASE

A. Cavity design

The first cavity we consider, called cavity π, is pictured in Fig. 2(a) and contains three posts. It is based on the design of a two-post re-entrant cavity from Refs. [23,24], and it possesses similar eigenmodes. The distributions of the magnetic fields of the two cavity eigenmodes of interest were simulated using COMSOL Multiphysics® [see Figs. 2(c) and 2(e)]. The magnetic fields of these two cavity eigenmodes are concentrated between the posts, where we place two identical YIG spheres of diameter 470 μm. Importantly, the magnetic fields of the eigenmodes are either in the same or opposite directions at the sphere locations, which leads to different coupling phases. This difference can also be understood by considering the strength and direction of the electric field, which is concentrated between the tops of the posts and the lid [see Figs. 2(b) and 2(d)]. For instance, the electric field of the first cavity eigenmode [see Fig. 2(b)] is localized only on the left and right posts, but with opposing directions [which, by the right-hand rule, agrees with the circulation of the magnetic field shown in Fig. 2(c)]. Conversely, for the second cavity eigenmode, the electric field is nonzero on top of each post, albeit with different intensities and orientations, and this leads to the magnetic field of Fig. 2(e).

B. Prediction of the physical phase

The numerical evaluation of the coupling strengths and coupling phases [given by Eqs. (1) and (2)] can be performed using eigenmode analysis in COMSOL Multiphysics, the results of which are summarized in Table I. Recall that the first index corresponds to the cavity mode, while the second is for the magnon mode. For the magnon modes, $l = 1$ ($l = 2$) corresponds to the left (right) YIG sphere. We first note that the coupling phases indeed follow

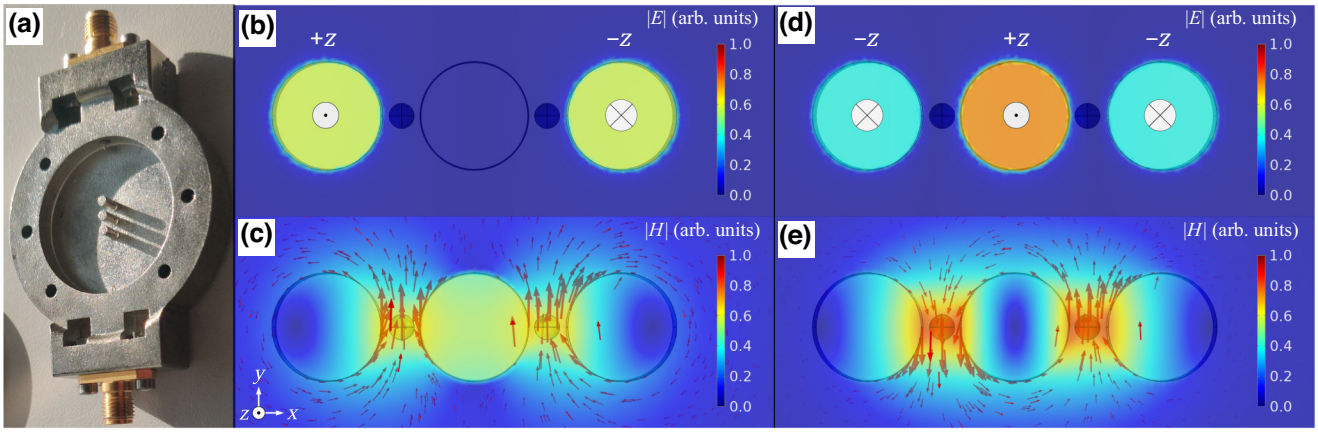

FIG. 2. (a) Three-post re-entrant cavity π used in the experiment. The lid of the cavity is not shown. (b),(c) Electric and magnetic field norms, simulated using COMSOL Multiphysics, of the first eigenmode c_1 (frequency $\omega_{c,1}/2\pi = 4.524$ GHz) of cavity π. (d),(e) Electric and magnetic field distributions, simulated using COMSOL, of the second eigenmode c_2 (frequency $\omega_{c,2}/2\pi = 6.378$ GHz) of cavity π. For each mode, the magnetic field is maximal between the posts, where the YIG spheres are placed, while the electric field is concentrated between the top of the posts and the lid of the cavity. The vectors are only shown for the magnetic field.

the directions of the two cavity eigenmodes' magnetic fields shown in Fig. 2. Furthermore, we observe that both YIG spheres couple with the same coupling strength to each cavity mode, as can be expected from the symmetry of the problem. Hence, from now on, we set $g_{11} = g_{12} = g_1$ and $g_{21} = g_{22} = g_2$. Assuming both YIG spheres to be perfectly identical, the Hamiltonian of the system is $H_\pi = H_{\text{free}} + H_I$, with

$$H_{\text{free}} = \sum_{k=1}^{2} \hbar\omega_{c,k} c_k^\dagger c_k + \sum_{l=1}^{2} \hbar\omega_m m_l^\dagger m_l, \tag{7}$$

where $\omega_m = \gamma H_0$ is the ferromagnetic resonance frequency of the lowest-order magnon modes (Kittel mode) and

$$\begin{aligned} H_I = {} & \hbar g_1 e^{-i\frac{\pi}{2}} c_1 m_1^\dagger + \hbar g_1 e^{-i\frac{\pi}{2}} c_1 m_2^\dagger \\ & + \hbar g_2 e^{i\frac{\pi}{2}} c_2 m_1^\dagger + \hbar g_2 e^{-i\frac{\pi}{2}} c_2 m_2^\dagger + \text{H.c.}, \end{aligned} \tag{8}$$

in which H.c. indicates the Hermitian conjugate terms. This system falls within the example of Fig. 1 by setting $g_3 = 0$, from which we deduce that after the unitary transformations, the interaction Hamiltonian can be written as

$$\begin{aligned} H_I = {} & \hbar g_1 c_1 m_1^\dagger + \hbar g_1 e^{i\theta_1} c_1 m_2^\dagger \\ & + \hbar g_2 c_2 m_1^\dagger + \hbar g_2 c_2 m_2^\dagger + \text{H.c.}, \end{aligned} \tag{9}$$

with $\theta_1 = \varphi_{12} - \varphi_{11} - (\varphi_{22} - \varphi_{21}) = \pi$; hence the name "cavity π" for the cavity.

The values of the coupling strengths and of the physical phase can be verified by the transmission amplitude $|S_{21}|$ through the cavity. Hence, in Appendix A, we present a frequency-domain simulation using COMSOL Multiphysics to numerically compute $|S_{21}|$ as a function of the magnon resonance frequency $\omega_m/2\pi$, and the results have good agreement with the eigenmode results of Table I.

C. Experimental results

The three-post cavity π design was 3D printed and then metallized. Using a vector network analyzer, we measured the transmission through the cavity when the static magnetic field $\mathbf{H}_0$ was swept to tune ω_m, and we obtained the data shown in Fig. 3. The hybridized photon-magnon polariton frequencies are predicted by the spectrum of $H_\pi = H_{\text{free}} + H_I$, with H_{free} given by Eq. (7) and H_I given by Eq. (9), and these are plotted on top of the color map with $\theta_1 = \pi$ as suggested by Table I, but with the adjusted parameters $g_1/2\pi = 81$ MHz and $g_2/2\pi = 120$ MHz instead. We attribute the difference between theory and experiment for the coupling strengths to the imperfection of the 3D printing and metallization processes. In particular, the three posts of cavity π are not completely cylindrical, which changes the focusing of the magnetic field between them.

TABLE I. Numerical calculation of the coupling strengths g_{kl} and coupling phases φ_{kl} of cavity π using COMSOL Multiphysics.

Coupling strength (MHz)		Coupling phase (rad)	
$g_{11}/2\pi$	139	φ_{11}	$-\frac{\pi}{2}$
$g_{12}/2\pi$	139	φ_{12}	$-\frac{\pi}{2}$
$g_{21}/2\pi$	207	φ_{21}	$+\frac{\pi}{2}$
$g_{22}/2\pi$	207	φ_{22}	$-\frac{\pi}{2}$

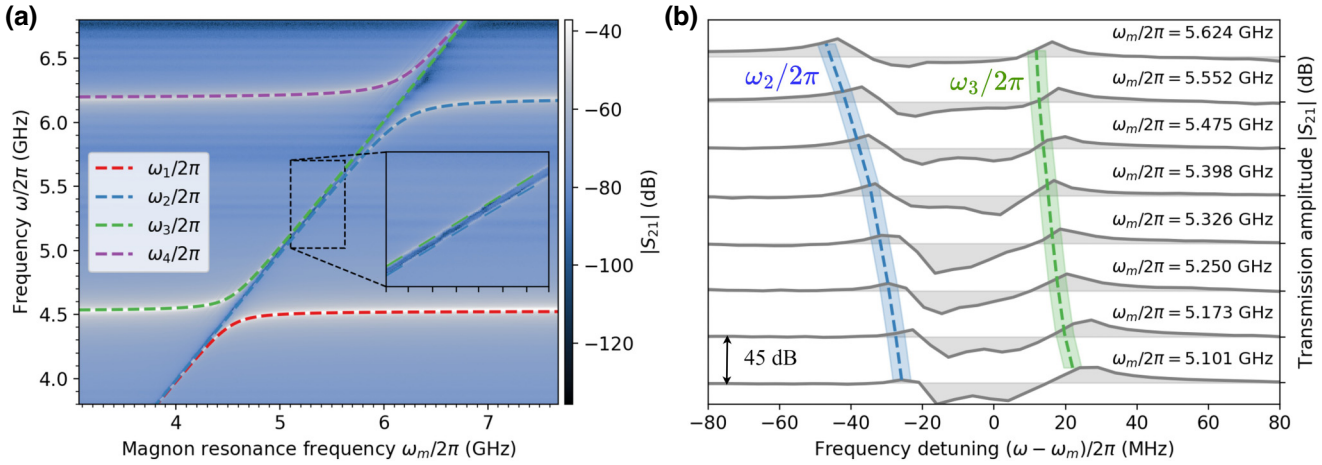

FIG. 3. (a) Experimental transmission amplitude $|S_{21}|$ of cavity π, along with the theoretical spectrum in dashed lines. The fit parameters are $\omega_{c,1}/2\pi = 4.527$ GHz, $\omega_{c,2}/2\pi = 6.19$ GHz, $g_1/2\pi = 81$ MHz, $g_2/2\pi = 120$ MHz, and $\theta_1 = \pi$. Inset: enlargement of $5.1 \leq \omega_m/2\pi \leq 5.62$ GHz, and $5.02 \leq \omega/2\pi \leq 5.7$ GHz, showing that the hybridized photon-magnon polariton frequencies $\omega_2/2\pi$ and $\omega_3/2\pi$ do not cross. The ticks on the base of the inset indicate the $\omega_m/2\pi$ cuts plotted in (b). (b) Line cuts for different values of $\omega_m/2\pi$ of the transmission amplitude $|S_{21}|$ with the spectrum in dashed lines. The width of $\omega_/2\pi$ and $\omega_3/2\pi$ show the uncertainty ± 2.5 MHz in frequency. For each line cut, the average value of the transmission is used to define the horizontal line from which the coloring begins: this allows resonances and antiresonances to be distinguished. All the transmission-line cuts are separated by 45 dB. The legend for the spectrum is common to (a) and (b).

Nevertheless, we note that while the observed coupling strengths are lower than the theoretical values, the prediction for θ_1 remains valid. Indeed, as shown in Ref. [43], the frequencies $\omega_2/2\pi$ and $\omega_3/2\pi$ cross for $\theta_1 = 0$, whereas they do not for $\theta_1 = \pi$. Figure 3(b) and the inset of Fig. 3(a) confirm the existence of a frequency gap between $\omega_2/2\pi$ and $\omega_3/2\pi$, which is the signature of the indirect coupling between both magnons, simultaneously mediated by the two cavity modes [43]. In other words, this spectral feature demonstrates the coherent coupling between two spatially distant YIG spheres mediated by the two cavity modes, despite the relatively high-frequency detuning. Note that if we instead had $\theta_1 = 0$, the indirect magnon-magnon coupling induced by each cavity mode would interfere destructively.

The coherent coupling of a cavity mode to two YIG spheres leads to an enhancement of the frequency gap at the anticrossings by $\sqrt{2}$; i.e., the gap is given by $2\sqrt{2}g$ instead of $2g$ [43,61], which we verify in Appendix B by comparison with measurements with a single YIG sphere. In addition, by examining the linewidths, we measured $\kappa_1/2\pi = 15 \pm 2.5$ MHz and $\kappa_2/2\pi = 22.5 \pm 2.5$ MHz for the linewidths of the cavity modes, and $\kappa_m/2\pi = 5 \pm 2.5$ MHz for the YIG spheres.

IV. ANALYSIS OF TWO PHYSICAL PHASES

A. Cavity $\pi 0$ design

Using cavity π, we showed the existence of a single physical phase $\theta_1 = \pi$. In this section, we examine the possibility of obtaining a different value for the physical phase. In the previous cavity, the origin of the difference in circulation of the magnetic field between the posts can be understood by examining the distribution of the electric field. Following this principle, we engineered another three-post re-entrant cavity to obtain two different values $\theta = 0$ and $\theta = \pi$ for the physical phases in a unique cavity. This is achieved by making the radius of the center post (0.75 mm) larger than that of the other two posts (0.5 mm), as shown in Fig. 4. As a result of this difference in the radii, the electric field intensity is stronger on the center post than on the other two [see Fig. 4(a)]. This leads to the appearance of another cavity eigenmode of frequency $\omega_{c,2}/2\pi = 7.525$ GHz, in which the magnetic field distribution rotates solely around the center post, as shown in Fig. 4(b). Interestingly, the other two cavity eigenmodes observed for cavity π remain, but their frequencies are modified as $\omega_{c,1}/2\pi \mapsto \omega_{c,1}/2\pi = 6.544$ GHz and $\omega_{c,2}/2\pi \mapsto \omega_{c,3}/2\pi = 8.567$ GHz.

B. Prediction of the physical phases

The resulting system consists of three cavity eigenmodes, each coupling to the two YIG spheres. The coupling strengths and coupling phases were computed using COMSOL Multiphysics, and the results are listed in Table II. Once again, given the symmetry of the problem, both YIG spheres couple with almost equal coupling strength to each cavity eigenmode, so we set $g_{11} = g_{12} = g_1 = 130$ MHz, $g_{21} = g_{22} = g_2 = 150$ MHz, and $g_{31} = g_{32} = g_3 = 104$ MHz. The system thus obtained is that described in Sec. II, and using Fig. 1, we deduce that the

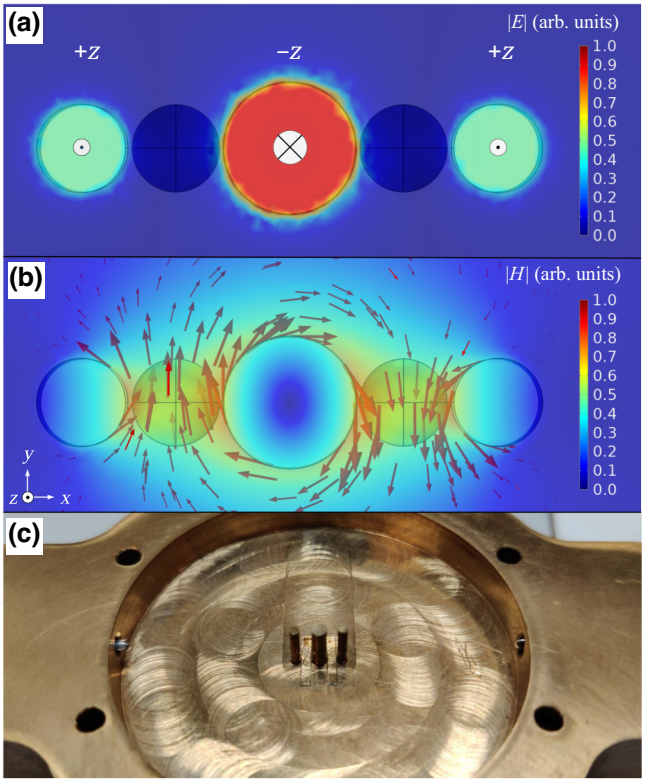

FIG. 4. (a) Electric and (b) magnetic field distributions, simulated using COMSOL Multiphysics, of the second eigenmode c_2 of cavity $\pi 0$. The two eigenmodes of cavity π still exist but have different frequencies. (c) Three-post re-entrant cavity $\pi 0$. In contrast to cavity π, the three posts do not have the same radius, leading to the creation of an additional cavity mode, as shown in (a),(b).

physics is characterized by two coupling phases θ_1 and θ_2. Using Table II, we predict $\theta_1 = \varphi_{12} - \varphi_{11} - (\varphi_{22} - \varphi_{21}) = \pi$ and $\theta_2 = \varphi_{32} - \varphi_{31} - (\varphi_{22} - \varphi_{21}) = 0$; hence the name "cavity $\pi 0$." The results of the frequency-domain simulation are presented in Appendix A, and they agree with the eigenmode analysis of Table II.

TABLE II. Numerical calculation of the coupling strengths g_{kl} and coupling phases φ_{kl} of cavity $\pi 0$ using COMSOL Multiphysics.

Coupling strength (MHz)		Coupling phase (rad)	
$g_{11}/2\pi$	130	φ_{11}	$-\frac{\pi}{2}$
$g_{12}/2\pi$	127	φ_{12}	$-\frac{\pi}{2}$
$g_{21}/2\pi$	148	φ_{21}	$+\frac{\pi}{2}$
$g_{22}/2\pi$	150	φ_{22}	$-\frac{\pi}{2}$
$g_{31}/2\pi$	103	φ_{31}	$+\frac{\pi}{2}$
$g_{32}/2\pi$	104	φ_{32}	$-\frac{\pi}{2}$

C. Experimental results

For cavity π of Sec. III, we did not have precise qualitative agreement with the theoretical predictions due to the additive manufacturing process of the cavity. Thus, we adopted a different strategy for cavity $\pi 0$: we used brass cylinders with a calibrated height to create the posts, and we machined the rest of the cavity from brass. In re-entrant cavities, the eigenmodes are very sensitive to the distance between the top of the posts and the lid. Hence, by using posts with identical heights, we ensured that the potential errors in the distance between the posts and the lid are uniform.

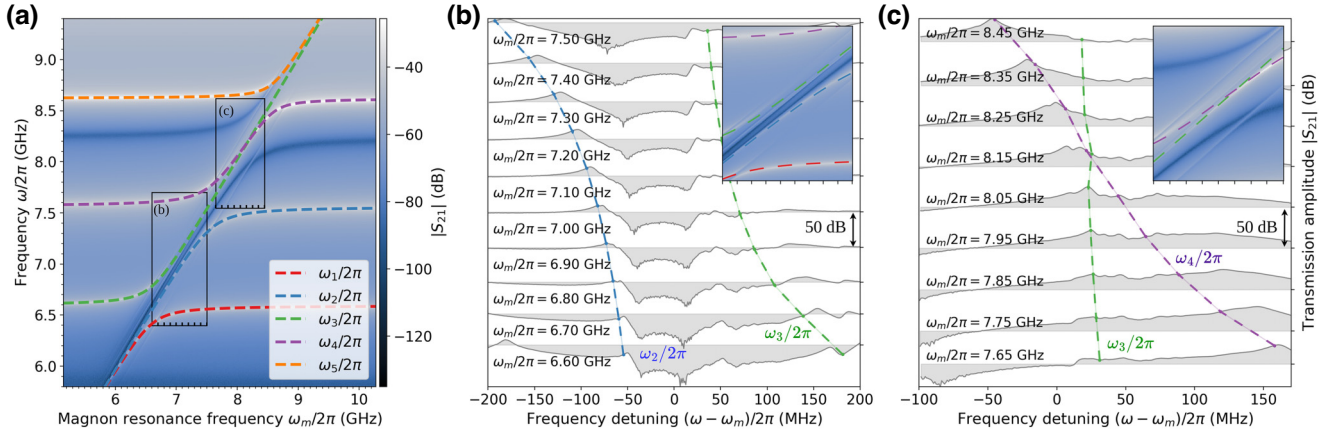

FIG. 5. (a) Experimental transmission amplitude ($|S_{21}|$) of cavity $\pi 0$, with the theoretical spectrum in dashed lines. The two rectangles show the data ranges used in (b),(c), with the ticks on the bottom indicating the $\omega_m/2\pi$ cuts. (b),(c) Transmission-amplitude cuts for different $\omega_m/2\pi$ values, with the spectrum in dashed lines. As in Fig. 3(b), the average value of the transmission is used to define the horizontal line from which the coloring begins. The fit parameters are indicated in Table II with the cavity resonances $\omega_{c,1}/2\pi = 6.594$ GHz, $\omega_{c,2}/2\pi = 7.562$ GHz, and $\omega_{c,3}/2\pi = 8.619$ GHz. The legend is common to all three subfigures, and the curves are all offset by 50 dB.

The experimental data, along with the polariton spectrum, are plotted in Fig. 5. This time, the fit parameters exactly correspond to those given in Table II, which indicates that the construction of the cavity matches very well with the COMSOL design. As for cavity π, the physical phase $\theta_1 = \pi$ suggests that the eigenfrequencies do not cross between the first two anticrossings, which is indeed confirmed by Fig. 5(b). On the other hand, having $\theta_2 = 0$ should lead to a crossing of the eigenfrequencies between the second and third anticrossings [43]; however, when $\theta_2 = 0$, one of the polaritons is a magnonic dark mode [39,43], which does not lead to a resonance in the transmission amplitude [61]. Thus, as seen in Fig. 5(c), we merely observe a single resonance peak moving as $\omega_m/2\pi$ is varied. This is verified using the input-output formalism [62] in Appendix C.

Compared with cavity π, we notice the appearance of higher-order magnon modes, which manifest as anticrossings located away from the magnon resonance $\omega_m/2\pi$. The excitation of these higher-order magnonic modes can be explained by the fact that the spheres used in this experiment are larger (radius of 0.5 mm, similar to the radius of the left and right posts; see Fig. 4), and thus the cavity modes' magnetic fields of Fig. 4(b) are less uniform over the spheres. The presence of a higher-order magnon mode can be verified by placing a single YIG sphere in cavity $\pi 0$ (see Fig. 9 in Appendix B). Finally, as shown in Appendix B, we also observe the $\sqrt{2}$ enhancement of the frequency gap at the anticrossings due to the coherent coupling of the two distant spin ensembles. The measured linewidths of the cavity modes are $\kappa_1/2\pi = 17 \pm 0.5$ MHz, $\kappa_2/2\pi = 42.5 \pm 0.5$ MHz, and $\kappa_3/2\pi = 20 \pm 0.5$ MHz. For the YIG spheres, we found the linewidths $\kappa_m/2\pi = 5 \pm 0.5$ MHz.

V. CONCLUSION

To summarize our results, we have proposed using three-post re-entrant cavities to engineer the coupling phases, and this leads to the engineering of synthetic gauge fields. The experimental data were shown to match with numerical predictions based on the theory developed in Ref. [43]. Depending on the value of the physical phase θ, which parametrizes the physics, we observe either a cavity-mediated magnon-magnon coupling ($\theta = \pi$) or dark-mode physics ($\theta = 0$). These findings are relevant for indirect coupling applications [14,21,22], dark-mode memories [39], and the creation of nonreciprocal behaviors [55,56,60]. While we focused on the the two cases $\theta \in \{0, \pi\}$, intermediate values of θ can be engineered using additional posts, as theoretically demonstrated in Appendix D.

Concerning indirect coupling, we verified the $\sqrt{2}$ enhancement of the coupling strength due to having two distant macroscopic spin ensembles coherently coupling with the cavity mode. In the case of $\theta = \pi$, the magnon-magnon coupling extends in the dispersive regime, where both magnons are strongly detuned from the cavity modes. As shown in Ref. [43], this results from the constructive interference of the cavity-mediated coupling by both cavity modes (while for $\theta = 0$, the cavity-mediated couplings interfere destructively). It was shown that the dispersive regime is advantageous for sensing applications based on magnons (i.e., magnetometry [63] or dark-matter detection [64]), so these schemes could benefit from engineering of the coupling phases.

This flexibility in the cavity-mediated coupling can also be useful for coupling magnons with superconducting transmon qubits through the cavity modes, which has so far only been demonstrated in rectangular cavities [16–19]. Indeed, such qubits couple to the electric field of the cavity modes, which in re-entrant cavities is focused on top of the posts [see Figs. 2(b), 2(d), and 4(a)]. The existence of several cavity modes, which may or may not couple to the magnons, is thus interesting for developing quantum information processing.

Finally, note that here the gauge-invariant phase θ parametrizing the synthetic gauge field is fixed by the coupling phases, which are themselves uniquely determined by the geometry of the cavity; nonetheless, tunability could be achieved by modulating the frequencies of one or more magnons [56], for instance by directly driving a YIG sphere using a loop generating a magnetic field parallel to the static magnetic field. Hence, in principle, re-entrant cavities can be used to engineer a loop-coupled system, and by tuning the gauge-invariant phases, either through cavity engineering or driving the YIG spheres, we

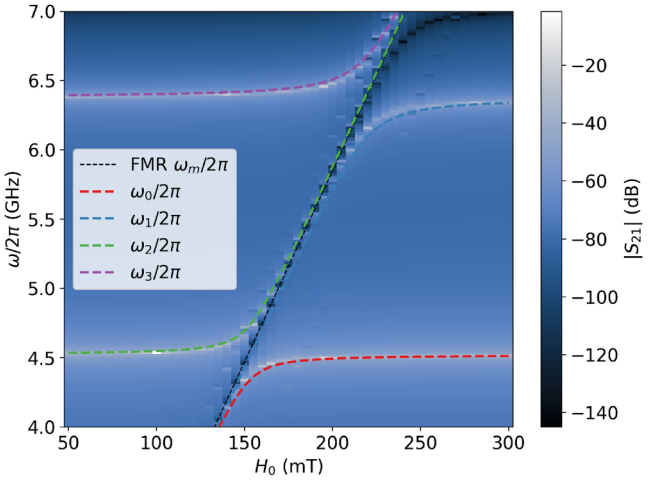

FIG. 6. Frequency-domain simulation, using COMSOL Multiphysics, of the transmission through cavity π. The spectra predicted using the eigenmode analysis of COMSOL Multiphysics are plotted on top, with the eigenfrequencies given in Fig. 2 and the other parameters given by Table I.

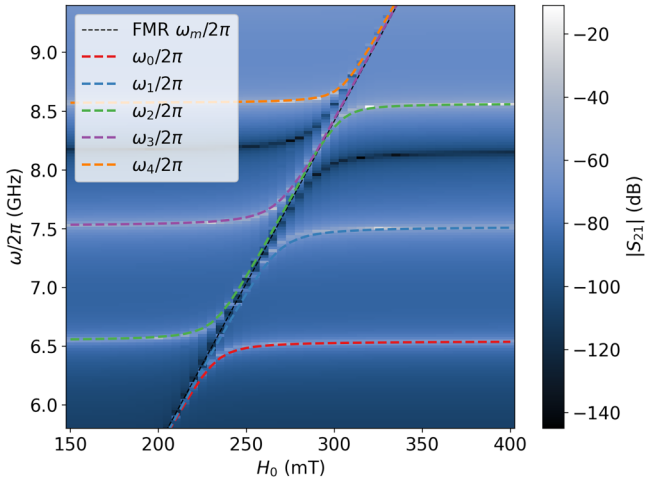

FIG. 7. Frequency-domain simulation, using COMSOL Multiphysics, of the transmission through cavity $\pi 0$. The spectra predicted using the eigenmode analysis of COMSOL Multiphysics are plotted on top, with the eigenfrequencies given in Sec. IV of the main text and the other parameters given by Table II.

could steer the system toward either cavity-mediated or dark-mode memory applications on demand.

ACKNOWLEDGMENTS

We would like to thank Bernard Abiven, mechanic at IMT Atlantique, for building cavity $\pi 0$. We acknowledge financial support from Thales Australia and Thales Research and Technology. This work is part of the research program supported by the European Union through the European Regional Development Fund (ERDF), by the Ministry of Higher Education and Research, Brittany and Rennes Métropole, through the CPER SpaceTech DroneTech, by Brest Métropole, and the ANR projects ICARUS and MagFunc. Jeremy Bourhill is funded by the Australian Research Council Centre of Excellence for Engineered Quantum Systems, CE170100009 and the Centre of Excellence for Dark Matter Particle Physics,

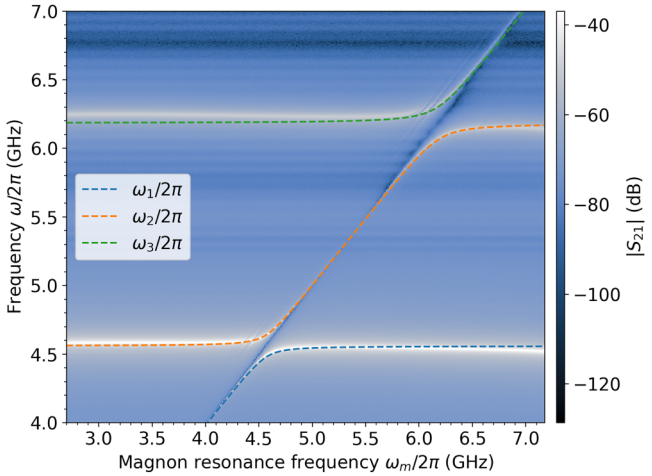

FIG. 8. Experimental transmission amplitude ($|S_{21}|$) of cavity π loaded with a single YIG sphere instead of two, with the theoretical spectrum in colored lines. The fit parameters are identical to those of Fig. 3(a) except for a shift of the first cavity mode, which was instead set to $\omega_{c,1}/2\pi = 4.56$ GHz.

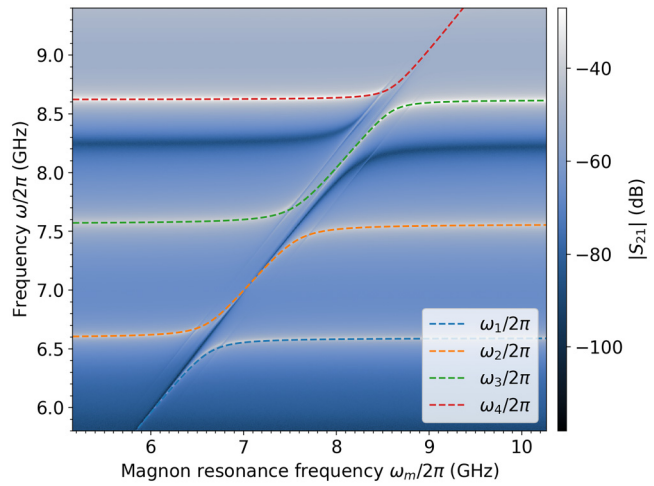

FIG. 9. Experimental transmission amplitude ($|S_{21}|$) of cavity $\pi 0$ loaded with a single YIG sphere instead of two, with the theoretical spectrum in colored lines. The fit parameters are exactly the same as those in Fig. 5.

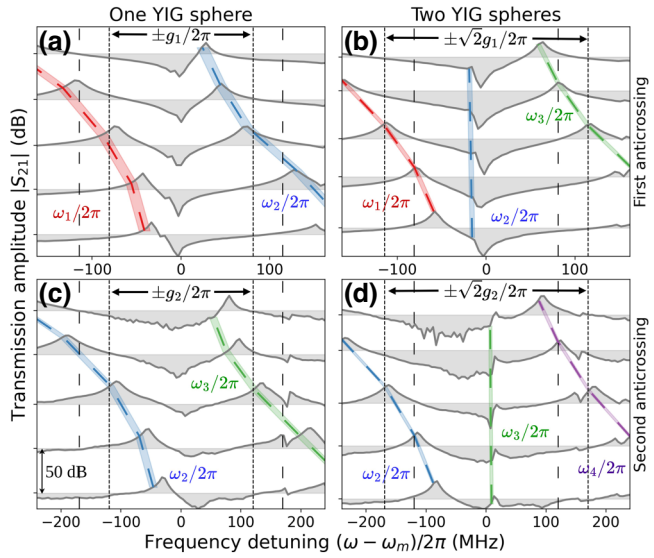

FIG. 10. Experimental transmission amplitude $|S_{21}|$ of cavity π for (a),(b) the first anticrossing and (c),(d) the second anticrossing. In the left column, we show the results for a single YIG sphere present in the cavity, while in the right column we show the case of two YIG spheres. From bottom to top, the line cuts in each subfigure are shown at $\omega_m \in \{\omega_{c,k} - 2g_k, \omega_{c,k} - g_k, \omega_{c,k}, \omega_{c,k} + g_k, \omega_{c,k} + 2g_k\}$. In all the subfigures, the curves are offset by 50 dB.

CE200100008. The scientific color map *oslo* [65] is used in this study to prevent visual distortion of the data and exclusion of readers with color-vision deficiencies [66].

APPENDIX A: SIMULATION RESULTS

In this appendix, we compare the simulation results of the eigenmode and frequency-domain analyses of COMSOL Multiphysics. The eigenmode simulations give the values of the coupling strengths and physical phases presented in Tables I and II, while the frequency-domain simulations give the transmission coefficient S_{21}. We use the results of the eigenmode analysis to plot the spectrum on top of the frequency-domain simulations, and we obtain good agreement, as shown in Fig. 6 for cavity π and Fig. 7 for cavity $\pi 0$.

Importantly, the frequency-domain COMSOL Multiphysics simulations only include the Kittel mode for the magnons and not higher-order modes; therefore, the presence of crossings (anticrossings) of the polaritonic frequencies for $\theta = 0$ ($\theta = \pi$) observed cannot be due to the presence of higher-order modes.

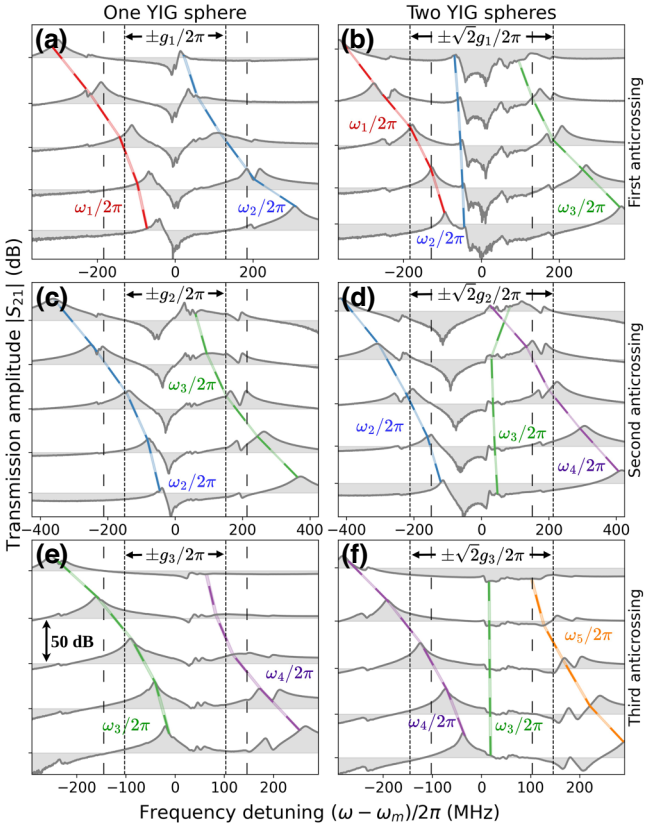

FIG. 11. Experimental transmission amplitude $|S_{21}|$ of cavity $\pi 0$ for (a),(b) the first anticrossing, (c),(d) the second anticrossing, and (e),(f) the third anticrossing. The line cuts are identical to those of Fig. 10.

APPENDIX B: COHERENT COUPLING OF TWO DISTANT SPHERES

The coherent coupling of N YIG spheres to a cavity mode leads to an enhancement by $\sqrt{N}$ of the frequency gap when the magnons are on resonance with the cavity mode [39]. To check that this was indeed the case, we removed one of the YIG spheres and measured cavities π and $\pi 0$ again. The experimental results are given in Fig. 8 for cavity π and in Fig. 9 for cavity $\pi 0$. We can notice the presence of higher-order magnon modes in both figures, which are characterized by diagonal lines parallel to the Kittel mode's frequency $\omega/2\pi$.

In Fig. 10, we compare the anticrossings for cavity π when a single YIG sphere is loaded in the cavity [Figs. 10(a) and 10(c)], versus two YIG spheres

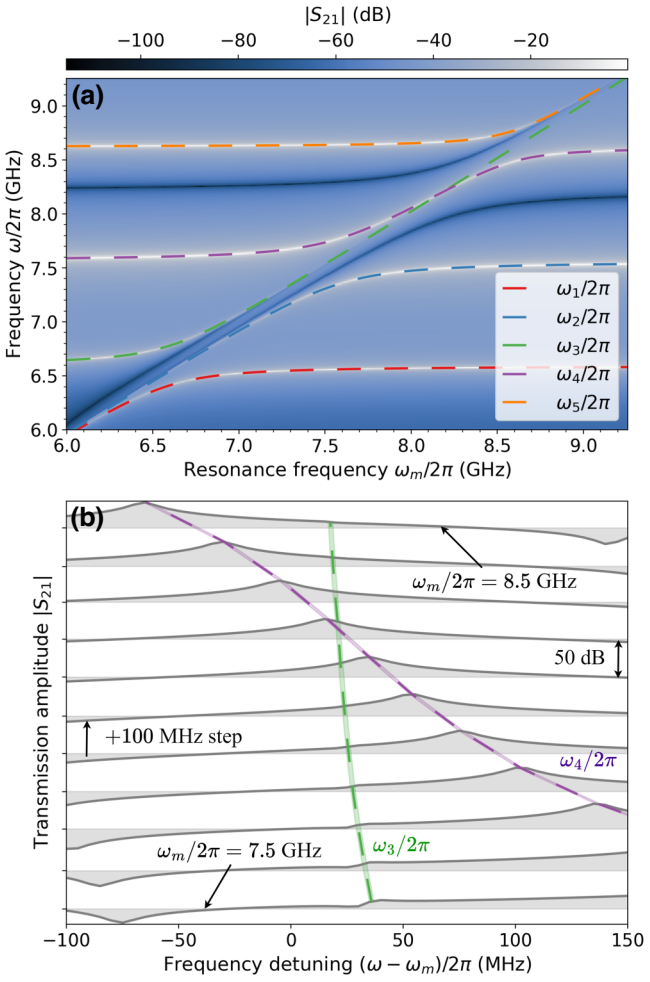

FIG. 12. Input-output modeling of the transmission amplitude $|S_{21}|$ through cavity $\pi 0$. (a) Transmission amplitude reproducing the experimental results of Fig. 5(a). (b) Cuts from $\omega_m/2\pi = 7.5$ GHz (bottom) up to $\omega_m/2\pi = 8.5$ GHz, in steps of 100 MHz, of the transmission amplitude $|S_{21}|$. These results mirror the experimental data of Fig. 5(c) and show the crossing of eigenvalues characteristic of $\theta_1 = 0$.

[Figs. 10(b) and 10(d)]. The dashed colored lines track the polariton frequencies, and these are seen to follow the resonance peaks. In particular, the third line cut corresponds to the magnon(s) being on resonance with the cavity mode, for which the anticrossing frequency gap is minimum. We see that in the case of a single YIG sphere, this frequency gap is given by $2g_k/2\pi$ (first column), whereas for two YIG spheres, the gap is $2\sqrt{2}g_k/2\pi$ (second column).

We carried out the same analysis for cavity $\pi 0$, as shown in Fig. 11, and the $\sqrt{2}$ enhancement was also verified. In Fig. 11(f), the vertical lines indicating $\pm\sqrt{2}g_3$ seem to be offset to the left. Note that if a YIG sphere is removed, the system is no longer loop coupled, and thus the effects of the coupling phases disappear.

APPENDIX C: INPUT-OUTPUT THEORY

The main objective of this appendix is to show that the dark mode arising for $\theta_2 = 0$ in cavity $\pi 0$ does not lead to a resonance in the transmission spectrum. To model the transmission amplitude $|S_{21}|$ through the cavity, we use the input-output formalism [62], for which there is abundant literature (see Refs. [11–13] for instance). The derivation is rather lengthy [43], and we therefore only describe the main steps here and refer the reader to Ref. [67] for more details.

To model the intrinsic dissipation of the magnon modes in the YIG spheres, we couple each of them to a bosonic bath with a real-valued and frequency-independent coupling rate $\kappa_m/2\pi = 5$ MHz (assumed to be identical for both YIG spheres). For the cavity modes, we only need to consider the two ports of the cavity, from which the S parameters are measured; therefore, we assume that the cavity mode c_i couples to two bosonic baths with frequency-independent coupling rates $\kappa_{ij}e^{i\phi_{ij}}/2\pi$, where $j \in \{1,2\}$ indexes the bath. Note that the phases ϕ_{ij} are necessary to reproduce the antiresonance behaviors, as recently shown in Ref. [67].

We use $\kappa_{1j}/2\pi = 1$ MHz, $\kappa_{2j}/2\pi = 3$ MHz, and $\kappa_{3j}/2\imath = 2$ MHz for $j \in \{1,2\}$. The values of the phases ϕ_{ij} can be obtained by examining the direction of the magnetic field (for instance, using an eigenmode analysis in COMSOL Multiphysics) coupled to the probes used to inject and measure the microwaves inside the cavity [67]. We set $\phi_{1j} = \pi_{3j} = \pi$ for $j \in \{1,2\}$ n $\phi_{21} = \pi$ and $\phi_{22} = 0$. Furthermore, the features of antiresonances depend on several cavity modes, and to properly model the lowest-frequency antiresonance, we included a lower-frequency cavity mode with frequency $\omega_0/2\pi = 3$ GHz and the negative coupling rates $\kappa_{01}/2\pi = \kappa_{02}/2\pi = -5$ MHz to the ports. For the cavity resonance frequencies and coupling strengths, we use the same values as for Fig. 5.

The results are plotted in Fig. 12, and we note, in particular, that Fig. 12(a) successfully reproduces Fig. 5(a). In Fig. 12(b), we reproduce Fig. 5(c) in the absence of higher-order magnon modes. As a consequence, the tracking of the polaritonic frequencies is simplified, and we verify the crossing of the eigenvalues. Notably, $\omega_3/2\pi$ does not lead to a resonance near the crossing, since it corresponds to a magnon dark mode, as theoretically predicted in Ref. [43].

APPENDIX D: ENGINEERING ARBITRARY PHYSICAL PHASES

The objective of this investigation was to design a cavity capable of introducing a nontrivial phase between consecutive modes while operating in the strong-coupling regime. To that effect, we developed a re-entrant cavity with five posts, which additionally ensures uniform coupling strength across multiple YIG spheres. Furthermore, the phase relationship between the two modes is contingent upon the positioning of four posts within the cavity,

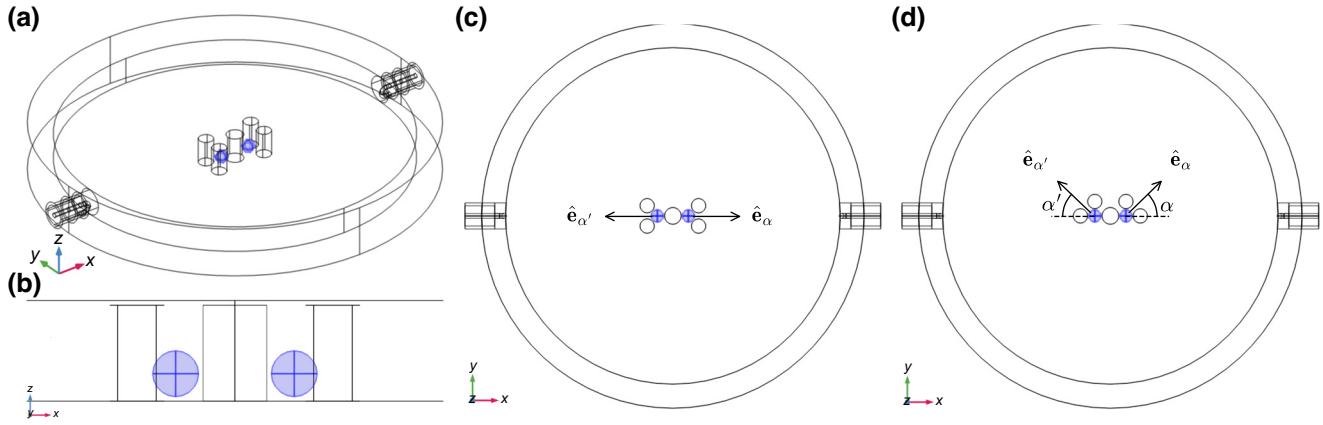

FIG. 13. Representation of the proposed re-entrant cavity (a) in three dimensions, (b) in the (z, x) plane enlarged to view the gap d between the tops of the posts and the lid, (c) in the (x, y) plane with the directions $\hat{\mathbf{e}}_\alpha$, $\hat{\mathbf{e}}_{\alpha'}$ represented, where $\hat{\mathbf{e}}_{\alpha'}$ is the mirror symmetry of $\hat{\mathbf{e}}_\alpha$ with respect to the (y, z) plane, and (d) in the (x, y) plane with the direction $\hat{\mathbf{e}}_\alpha$ making an angle α with respect to the x axis. The two YIG spheres are represented in blue.

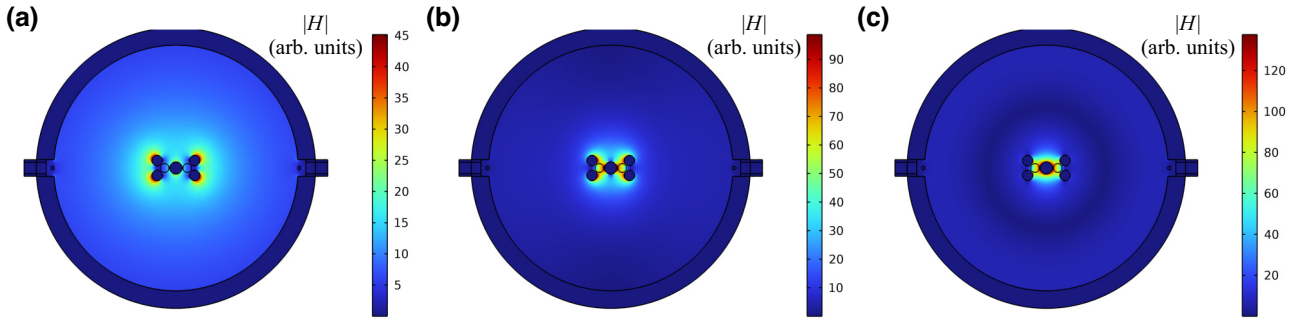

FIG. 14. Representation of the $|H|$ field of the first three cavity modes in the (x, y) plane at the z coordinate of the center of the YIG spheres.

as demonstrated in our analysis. By manipulating the positions of these posts, it is feasible to fine-tune the coupling phase by adjusting the gap between the top of the post and the cavity lid.

The cavity dimensions were optimized to maximize the coupling strength for each YIG sphere and to ensure that the phase falls within the range $[n(\pi/4), (n+1)(\pi/4)]$ with $n \in \mathbb{Z}$ by tuning an angle α, as detailed in the following. As depicted in Fig. 13, the cavity is cylindrical and features five cylindrical posts. The cavity has a radius of 14 mm and a height of 2.25 mm. All posts have the same height, which depends on the value of the gap d; thus, the post height is $2.25 - d$. Positioned at the center of the cavity is a fixed post with a radius of 0.7 mm. The two YIG spheres are located on either side of the center post along the x axis, with a spacing of 0.1 mm from the center post. Four additional posts are situated at the periphery of each YIG sphere, spaced 0.1 mm from the spheres. These peripheral posts are symmetrically positioned with respect to the y axis, which passes through the center of the cavity. The radius of the peripheral posts is 0.6 mm. Relative to the direction $\hat{e}_\alpha$, the two peripheral posts on the right-hand side of the cavity are positioned at $\pm 45°$. In addition, the direction $\hat{e}_\alpha$ forms an angle α with the x axis, ranging from $0°$ to $45°$, allowing the tuning of the coupling phases.

The norms of the cavity modes' magnetic fields are depicted in Fig. 14 for the first three modes of the cavity. We focus on the second and third modes due to their high filling factor η [see Eq. (3)], which are quite similar for both modes and spheres, as illustrated in Table III. This table presents the eigenfrequencies $\omega/2\pi$ of the first three modes of the cavity, along with the filling factors η_L and η_R for the YIG spheres on the left- and right-hand sides, respectively. In addition, the associated coupling strengths g_L and g_R are provided. The values are given for an angle $\alpha = 0°$ and a gap $d = 50$ μm.

Table IV presents similar characteristics for the two modes of interest, along with the averaged H-field direction inside each YIG sphere and the coupling phase. It is observed that the coupling strength slightly decreases from $\alpha = 0°$ to $\alpha = 45°$, whereas the difference in coupling strength between mode 1 and mode 2 slightly increases; however, the coupling strength remains relatively constant, ranging from 4.2% to 5.7%. The coupling phase varies between $129°$ and $180°$ for α ranging from $45°$ to $0°$, allowing for measurements with a nontrivial physical phase between $135°$ and $180°$.

TABLE III. Characteristics of the first three cavity modes for $d = 50$ μm.

Mode	$\omega/2\pi$ (GHz)	η_L	η_R	g_L/ω	g_R/ω
0	4.02	0.018	0.019	0.011	0.012
1	8.29	0.125	0.123	0.055	0.056
2	12.03	0.144	0.145	0.055	0.055

TABLE IV. Characteristics of the cavity modes versus α for $d = 50$ μm.

α (°)	$\omega/2\pi$ (GHz)	η_L	η_R	g_L/ω	g_R/ω	ϕ_L (°)	ϕ_R (°)	θ (°)
0	8.29	0.125	0.123	0.057	0.056	90	90	180
	12.03	0.144	0.145	0.055	0.055	−90	90	
5	8.29	0.125	0.122	0.057	0.056	−91	−88	170
	12.09	0.141	0.142	0.053	0.053	−86	87	
10	8.27	0.125	0.122	0.057	0.055	−92	−87	160
	12.07	0.139	0.140	0.053	0.053	−82	83	
15	8.33	0.124	0.122	0.056	0.055	86	95	151
	12.09	0.134	0.134	0.050	0.051	−79	80	
20	8.38	0.124	0.120	0.056	0.055	85	96	144
	12.07	0.130	0.130	0.049	0.049	−76	78	
25	8.48	0.122	0.121	0.055	0.054	−97	−83	139
	12.05	0.126	0.125	0.047	0.047	−76	77	
30	8.54	0.122	0.119	0.055	0.054	83	98	133
	12.03	0.121	0.121	0.046	0.046	−74	75	
35	8.62	0.121	0.119	0.054	0.053	−98	−81	131
	11.99	0.119	0.119	0.045	0.045	106	−105	
40	8.74	0.121	0.118	0.054	0.052	81	99	130
	11.97	0.115	0.115	0.044	0.044	−73	74	
45	8.90	0.120	0.118	0.053	0.052	−99	−80	128
	11.96	0.112	0.112	0.042	0.042	−74	74	

TABLE V. Characteristics of the cavity modes versus d for $\alpha = 45°$.

d (μm)	$\omega/2\pi$ (GHz)	η_L	η_R	g_L/ω	g_R/ω	ϕ_L (°)	ϕ_R (°)	θ (°)
5	3.34	0.123	0.116	0.088	0.083	80	102	146
	4.67	0.154	0.157	0.093	0.095	97	−95	
10	4.63	0.124	0.115	0.075	0.070	−100	−78	147
	6.45	0.155	0.158	0.080	0.082	97	−94	
25	6.88	0.122	0.118	0.061	0.059	−100	−79	144
	9.61	0.156	0.158	0.066	0.067	98	−97	
50	8.90	0.120	0.118	0.053	0.052	−99	−80	129
	11.95	0.112	0.112	0.043	0.043	−74	74	
100	10.84	0.112	0.110	0.045	0.044	82	98	90
	12.77	0.051	0.051	0.019	0.019	−53	53	

Table V presents the same information for a fixed angle of 45° while varying the gap d from 100 to 5 μm. This demonstrates that measurements with a nontrivial phase can be conducted within the range 90° to 135°.

[1] S. A. Wolf, D. D. Awschalom, R. A. Buhrman, J. M. Daughton, S. von Molnar, M. L. Roukes, A. Y. Chtchelkanova, and D. M. Treger, Spintronics: A spin-based electronics vision for the future, Science **294**, 1488 (2001).

[2] A. V. Chumak, V. I. Vasyuchka, A. A. Serga, and B. Hillebrands, Magnon spintronics, Nat. Phys. **11**, 453 (2015).

[3] G. Csaba, Á. Papp, and W. Porod, Perspectives of using spin waves for computing and signal processing, Phys. Lett. A **381**, 1471 (2017).

[4] A. V. Chumak, A. A. Serga, and B. Hillebrands, Magnonic crystals for data processing, J. Phys. D: Appl. Phys. **50**, 244001 (2017).

[5] A. V. Chumak, Fundamentals of magnon-based computing, arXiv:1901.08934.

[6] A. Barman, *et al.*, The 2021 magnonics roadmap, J. Phys.: Condens. Matter **33**, 413001 (2021).

[7] A. Mahmoud, F. Ciubotaru, F. Vanderveken, A. V. Chumak, S. Hamdioui, C. Adelmann, and S. Cotofana, Introduction to spin wave computing, J. Appl. Phys. **128**, 161101 (2020).

[8] S. Bhatti, R. Sbiaa, A. Hirohata, H. Ohno, S. Fukami, and S. Piramanayagam, Spintronics based random access memory: A review, Mater. Today **20**, 530 (2017).

[9] A. V. Chumak, *et al.*, Advances in magnetics roadmap on spin-wave computing, IEEE Trans. Magn. **58**, 1 (2022). working paper or preprint

[10] J. Grollier, D. Querlioz, K. Y. Camsari, K. Everschor-Sitte, S. Fukami, and M. D. Stiles, Neuromorphic spintronics, Nat. Electron. **3**, 360 (2020).

[11] M. Harder, B. M. Yao, Y. S. Gui, and C.-M. Hu, Coherent and dissipative cavity magnonics, J. Appl. Phys. **129**, 201101 (2021).

[12] B. Z. Rameshti, S. V. Kusminskiy, J. A. Haigh, K. Usami, D. Lachance-Quirion, Y. Nakamura, C.-M. Hu, H. X. Tang, G. E. Bauer, and Y. M. Blanter, Cavity magnonics, arXiv:2106.09312.

[13] H. Yuan, Y. Cao, A. Kamra, R. A. Duine, and P. Yan, Quantum magnonics: When magnon spintronics meets quantum information science, Phys. Rep. **965**, 1 (2022).

[14] D. Lachance-Quirion, Y. Tabuchi, A. Gloppe, K. Usami, and Y. Nakamura, Hybrid quantum systems based on magnonics, Appl. Phys. Express **12**, 070101 (2019).

[15] X. Zhang, C.-L. Zou, L. Jiang, and H. X. Tang, Cavity magnomechanics, Sci. Adv. **2**, e1501286 (2016).

[16] Y. Tabuchi, S. Ishino, A. Noguchi, T. Ishikawa, R. Yamazaki, K. Usami, and Y. Nakamura, Coherent coupling between a ferromagnetic magnon and a superconducting qubit, Science **349**, 405 (2015).

[17] Y. Tabuchi, S. Ishino, A. Noguchi, T. Ishikawa, R. Yamazaki, K. Usami, and Y. Nakamura, Quantum magnonics: The magnon meets the superconducting qubit, C. R. Phys. **17**, 729 (2016). quantum microwaves / Micro-ondes quantiques.

[18] D. Lachance-Quirion, Y. Tabuchi, S. Ishino, A. Noguchi, T. Ishikawa, R. Yamazaki, and Y. Nakamura, Resolving quanta of collective spin excitations in a millimeter-sized ferromagnet, Sci. Adv. **3**, e1603150 (2017).

[19] D. Lachance-Quirion, S. P. Wolski, Y. Tabuchi, S. Kono, K. Usami, and Y. Nakamura, Entanglement-based single-shot detection of a single magnon with a superconducting qubit, Science **367**, 425 (2020).

[20] N. Crescini, C. Braggio, G. Carugno, A. Ortolan, and G. Ruoso, Coherent coupling between multiple ferrimagnetic spheres and a microwave cavity at millikelvin temperatures, Phys. Rev. B **104**, 064426 (2021).

[21] N. J. Lambert, J. A. Haigh, S. Langenfeld, A. C. Doherty, and A. J. Ferguson, Cavity-mediated coherent coupling of magnetic moments, Phys. Rev. A **93**, 021803 (2016).

[22] P. Hyde, L. Bai, M. Harder, C. Match, and C.-M. Hu, Indirect coupling between two cavity modes via ferromagnetic resonance, Appl. Phys. Lett. **109**, 152405 (2016).

[23] M. Goryachev, W. G. Farr, D. L. Creedon, Y. Fan, M. Kostylev, and M. E. Tobar, High-cooperativity cavity QED with magnons at microwave frequencies, Phys. Rev. Appl. **2**, 054002 (2014).

[24] N. Kostylev, M. Goryachev, and M. E. Tobar, Superstrong coupling of a microwave cavity to yttrium iron garnet magnons, Appl. Phys. Lett. **108**, 062402 (2016).

[25] I. A. Golovchanskiy, N. N. Abramov, V. S. Stolyarov, A. A. Golubov, M. Y. Kupriyanov, V. V. Ryazanov, and A. V. Ustinov, Approaching deep-strong on-chip photon-to-magnon coupling, Phys. Rev. Appl. **16**, 034029 (2021).

[26] I. A. Golovchanskiy, N. N. Abramov, V. S. Stolyarov, M. Weides, V. V. Ryazanov, A. A. Golubov, A. V. Ustinov, and M. Y. Kupriyanov, Ultrastrong photon-to-magnon coupling in multilayered heterostructures involving superconducting coherence via ferromagnetic layers, Sci. Adv. **7**, eabe8638 (2021).

[27] G. Bourcin, J. Bourhill, V. Vlaminck, and V. Castel, Strong to ultra-strong coherent coupling measurements in a YIG/cavity system at room temperature, arXiv:2209.14643.

[28] W. Yu, J. Wang, H. Y. Yuan, and J. Xiao, Prediction of attractive level crossing via a dissipative mode, Phys. Rev. Lett. **123**, 227201 (2019).

[29] J. Zhao, Y. Liu, L. Wu, C.-K. Duan, Y. x. Liu, and J. Du, Observation of anti-$\mathcal{PT}$-symmetry phase transition in the magnon-cavity-magnon coupled system, Phys. Rev. Appl. **13**, 014053 (2020).

[30] M. Harder, Y. Yang, B. M. Yao, C. H. Yu, J. W. Rao, Y. S. Gui, R. L. Stamps, and C.-M. Hu, Level attraction due to dissipative magnon-photon coupling, Phys. Rev. Lett. **121**, 137203 (2018).

[31] B. Bhoi, B. Kim, S.-H. Jang, J. Kim, J. Yang, Y.-J. Cho, and S.-K. Kim, Abnormal anticrossing effect in photon-magnon coupling, Phys. Rev. B **99**, 134426 (2019).

[32] Y. Yang, J. W. Rao, Y. S. Gui, B. M. Yao, W. Lu, and C.-M. Hu, Control of the magnon-photon level attraction in a planar cavity, Phys. Rev. Appl. **11**, 054023 (2019).

[33] B. Yao, T. Yu, X. Zhang, W. Lu, Y. Gui, C.-M. Hu, and Y. M. Blanter, The microscopic origin of magnon-photon level attraction by traveling waves: Theory and experiment, Phys. Rev. B **100**, 214426 (2019).

[34] B. Yao, T. Yu, Y. S. Gui, J. W. Rao, Y. T. Zhao, W. Lu, and C.-M. Hu, Coherent control of magnon radiative damping with local photon states, Commun. Phys. **2**, 161 (2019).

[35] Z. Lu, X. Mi, Q. Zhang, Y. Sun, J. Guo, Y. Tian, S. Yan, and L. Bai, Interference induced microwave transmission in the YIG-microstrip cavity system, J. Magn. Magn. Mater. **540**, 168457 (2021).

[36] Y.-P. Wang, J. W. Rao, Y. Yang, P.-C. Xu, Y. S. Gui, B. M. Yao, J. Q. You, and C.-M. Hu, Nonreciprocity and unidirectional invisibility in cavity magnonics, Phys. Rev. Lett. **123**, 127202 (2019).

[37] I. Boventer, M. Kläui, R. Macedo, and M. Weides, Steering between level repulsion and attraction: Broad tunability of two-port driven cavity magnon-polaritons, New J. Phys. **21**, 125001 (2019).

[38] I. Boventer, C. Dorflinger, T. Wolz, R. Macedo, R. Lebrun, M. Klaui, and M. Weides, Control of the coupling strength and linewidth of a cavity magnon-polariton, Phys. Rev. Res. **2**, 013154 (2020).

[39] X. Zhang, C.-L. Zou, N. Zhu, F. Marquardt, L. Jiang, and H. X. Tang, Magnon dark modes and gradient memory, Nat. Commun. **6**, 8914 (2015).

[40] X. Li, J. Li, X. Cheng, and G. Li, Nonreciprocal transmission in a four-mode cavity magnonics system, Laser Phys. Lett. **19**, 095208 (2022).

[41] N. Zhu, X. Han, C.-L. Zou, M. Xu, and H. X. Tang, Magnon-photon strong coupling for tunable microwave circulators, Phys. Rev. A **101**, 043842 (2020).

[42] C. Kong, J. Liu, and H. Xiong, Nonreciprocal microwave transmission under the joint mechanism of phase modulation and magnon Kerr nonlinearity effect, Front. Phys. **18**, 12501 (2022).

[43] A. Gardin, J. Bourhill, V. Vlaminck, C. Person, C. Fumeaux, V. Castel, and G. C. Tettamanzi, Manifestation of the coupling phase in microwave cavity magnonics, Phys. Rev. Appl. **19**, 054069 (2023).

[44] S. Zheng, F. Sun, Y. Lai, Q. Gong, and Q. He, Manipulation and enhancement of asymmetric steering via interference effects induced by closed-loop coupling, Phys. Rev. A **99**, 022335 (2019).

[45] J. Huang, D.-G. Lai, and J.-Q. Liao, Controllable generation of mechanical quadrature squeezing via dark-mode engineering in cavity optomechanics, Phys. Rev. A **108**, 013516 (2023).

[46] J. Koch, A. A. Houck, K. L. Hur, and S. M. Girvin, Time-reversal-symmetry breaking in circuit-QED-based photon lattices, Phys. Rev. A **82**, 043811 (2010).

[47] N. R. Bernier, L. D. Tóth, A. Koottandavida, M. A. Ioannou, D. Malz, A. Nunnenkamp, A. K. Feofanov, and T. J. Kippenberg, Nonreciprocal reconfigurable microwave optomechanical circuit, Nat. Commun. **8**, 604 (2017).

[48] K. Fang, J. Luo, A. Metelmann, M. H. Matheny, F. Marquardt, A. A. Clerk, and O. Painter, Generalized non-reciprocity in an optomechanical circuit via synthetic magnetism and reservoir engineering, Nat. Phys. **13**, 465 (2017).

[49] Y. Chen, Y.-L. Zhang, Z. Shen, C.-L. Zou, G.-C. Guo, and C.-H. Dong, Synthetic gauge fields in a single optomechanical resonator, Phys. Rev. Lett. **126**, 123603 (2021).

[50] T. Holstein and H. Primakoff, Field dependence of the intrinsic domain magnetization of a ferromagnet, Phys. Rev. **58**, 1098 (1940).

[51] G. Flower, M. Goryachev, J. Bourhill, and M. E. Tobar, Experimental implementations of cavity-magnon systems: From ultra strong coupling to applications in precision measurement, New J. Phys. **21**, 095004 (2019).

[52] J. Bourhill, V. Castel, A. Manchec, and G. Cochet, Universal characterization of cavity–magnon polariton coupling strength verified in modifiable microwave cavity, J. Appl. Phys. **128**, 073904 (2020).

[53] A. Frisk Kockum, A. Miranowicz, S. De Liberato, S. Savasta, and F. Nori, Ultrastrong coupling between light and matter, Nat. Rev. Phys. **1**, 19 (2019).

[54] A. Le Boité, Theoretical methods for ultrastrong light–matter interactions, Adv. Quantum Technol. **3**, 1900140 (2020).

[55] A. Metelmann and A. A. Clerk, Nonreciprocal photon transmission and amplification via reservoir engineering, Phys. Rev. X **5**, 021025 (2015).

[56] A. Clerk, Introduction to quantum non-reciprocal interactions: From non-Hermitian Hamiltonians to quantum master equations and quantum feedforward schemes, SciPost Phys Lect. Notes **44**, 44 (2022).

[57] Y.-J. Lin, R. L. Compton, K. Jiménez-García, J. V. Porto, and I. B. Spielman, Synthetic magnetic fields for ultracold neutral atoms, Nature **462**, 628 (2009).

[58] J. Dalibard, F. Gerbier, G. Juzeliūnas, and P. Ohberg, Colloquium: Artificial gauge potentials for neutral atoms, Rev. Mod. Phys. **83**, 1523 (2011).

[59] K. M. Sliwa, M. Hatridge, A. Narla, S. Shankar, L. Frunzio, R. J. Schoelkopf, and M. H. Devoret, Reconfigurable Josephson circulator/directional amplifier, Phys. Rev. X **5**, 041020 (2015).

[60] S.-A. Biehs and G. S. Agarwal, Enhancement of synthetic magnetic field induced nonreciprocity via bound states in the continuum in dissipatively coupled systems, Phys. Rev. B **108**, 035423 (2023).

[61] J. M. P. Nair, D. Mukhopadhyay, and G. S. Agarwal, Cavity-mediated level attraction and repulsion between magnons, Phys. Rev. B **105**, 214418 (2022).

[62] C. W. Gardiner and M. J. Collett, Input and output in damped quantum systems: Quantum stochastic differential equations and the master equation, Phys. Rev. A **31**, 3761 (1985).
[63] N. Crescini, G. Carugno, and G. Ruoso, Phase-modulated cavity magnon polaritons as a precise magnetic field probe, Phys. Rev. Appl. **16**, 034036 (2021).
[64] G. Flower, J. Bourhill, M. Goryachev, and M. E. Tobar, Broadening frequency range of a ferromagnetic axion haloscope with strongly coupled cavity–magnon polaritons, Phys. Dark Universe **25**, 100306 (2019).
[65] F. Crameri, Scientific colour maps, 2021.
[66] F. Crameri, G. E. Shephard, and P. J. Heron, The misuse of colour in science communication, Nat. Commun. **11**, 5444 (2020).
[67] G. Bourcin, A. Gardin, J. Bourhill, V. Vlaminck, and V. Castel, Level attraction in a quasi-closed cavity, arXiv:2402.06258.